Propagation of laser beams formed by unstable resonators with different magnifications

S. Saghafi, M.J. Withford, and J.A. Piper

Abstract: Laser beams generated from high-magnification on-axis unstable resonators using hard-edged axial scraper mirrors and output couplers consisting of axial spot reflectors typically have an annular distribution in the near field (i.e., a flat-top profile with a hole in the middle for an axially coupled beam). We employ a new model, based on the flattened Gaussian beam (FGB) concept, to describe the propagation of such annular near-field beams. The superposition of two FGBs, whose flatness and steepness of edges are controlled by defined parameters (i.e., the beam width and the order), is used to analyze the output beam intensity profile along the propagation axis. We apply this model to characterize the output beams of copper vapour lasers employing unstable resonators of different magnifications ($M = 80$, 200, and 400). We show that once the model is fitted to the beam intensity profile at any two positions along the axis of propagation, it can be used to predict the beam shape at any position.

PACS Nos.: 42.55.–f, 42.55.Lt, 42.60.–v

Résumé : Les faisceaux laser générés par des résonateurs axiaux instables à haute magnification et utilisant des mirroirs troués axiaux et des coupleurs de sortie faits de réflecteurs à tache axiale ont typiquement une distribution annulaire en champ proche (un profile aplati avec un trou dans le milieu pour le faisceau couplé axialement). Nous utilisons un nouveau modèle basé sur le concept des faisceaux gaussiens aplatis (FGB) pour décrire la propagation de tels faisceaux à champ proche annulaire. Nous utilisons la superposition de deux FGB dont l'épaisseur et la pente en bordure sont contrôlées par les paramètres les définissant (la largeur du faisceau et l'ordre), afin d'analyser le profile d'intensité du faisceau de sortie le long de l'axe de propagation. Nous appliquons le modèle à la caractérisation des faisceaux de sortie de lasers à vapeur de cuivre qui utilisent des résonateurs instables de différentes magnification ($M = 80$, 200 et 400). Nous montrons qu'une fois que le modèle est ajusté au profile d'intensité du faisceau en deux points de l'axe de propagation, il est capable de prédire la forme du faisceau en tout point.

[Traduit par la Rédaction]

Received 9 March 2005. Accepted 25 February 2006. Published on the NRC Research Press Web site at http://cjp.nrc.ca/ on 18 July 2006.

S. Saghafi.[1] Plasma-Physics Research Center, Science and Research Branch Campus, Islamic-Azad University, Tehran, Iran.
M.J. Withford and J.A. Piper. Department of Physics, Macquarie University, Sydney, NSW 2109, Australia.

[1]Corresponding author (e-mail: s-saghafi@cc.sbu.ac.ir).

 doi: 10.1139/P06-013

1. Introduction

Recently, a new computational model, the so-called flattened Gaussian beam with hole in the middle (FGBHM) model, was introduced that characterizes the output beam of lasers employing unstable resonators (UR) [1].

The FGBHM model is based on a superposition of standard Laguerre–Gaussian modes in the paraxial regime. It was shown that geometrical physics can be used to overcome problems arising when the angle of divergence of the beam exceeds (up to 15%) the output angle of divergence in the paraxial regime [1]. Extensive studies of beam evolution in high-gain pulsed lasers has shown that beam quality can be significantly improved by using high-magnification UR (the ratio of the high reflector's radius of curvature to the spot reflector's radius of curvature) [2]. In this paper, the FGBHM model with the intensity moment formalism (IMF) method are employed to characterize the output beam of a metal vapour laser employing UR with magnifications $M = 80, 200$, and 400. Using the IMF method, standard parameters such as the beam propagation factor M^2 and the kurtosis parameter k can be obtained that provide useful information about the beam width, the angle of divergence, and the beam's profile at any point along the z-axis [3–10].

As many lasers used for medical or industrial applications (i.e., material processing and related applications) have URs giving "flat-top with a central shadow" beams (e.g., Nd:YAG, Excimer, and copper vapour lasers) and since the quality of the output beam in these lasers is controlled by magnification, developing a unique method to characterize the output beam profiles of lasers employing URs of different magnification, from the theoretical and experimental points of view, is desirable.

2. Flattened Gaussian beams with a hole in the middle

In 1994, Gori introduced a new theoretical description for axially symmetric "flat-top" beams, termed flattened Gaussian beam (FGB) [11]. At the waist, the beam is described as a finite sum of Laguerre–Gaussian functions

$$\begin{aligned}\psi(r,0) &= A\sum_{n=0}^{N} C_n L_n\left(\frac{2Nr^2}{w_0^2}\right)\exp\left[\frac{-Nr^2}{w_0^2}\right] \\ &= A\sum_{n=0}^{N}\exp\left(-\frac{Nr^2}{w_0^2}\right)\frac{\left(Nr^2/w_0^2\right)^n}{n!}, \qquad N = 1, 2, 3, \ldots \end{aligned} \tag{1}$$

where A is a scale constant, w_0 the beam spot size, $C_n = (-1)^n \sum_{m=n}^{N} \binom{m}{n} \frac{1}{2^m}$, L_n is the generalized Laguerre function and N is the beam order that controls the flatness of the irradiance distribution [11]. The FGB model is the superposition of N Laguerre–Gaussian modes. The larger N becomes, the more rapid are the changes in the beam intensity profile as the beam propagates. Moreover, the shoulders of the near-field intensity distributions change (sharpen), effectively, for increasing beam order N, and for very large beam order a rectangular beam intensity profile can be obtained.

The output of lasers operating with on-axis, high-magnification UR, using axial scraper mirrors and spot reflectors have annular near-field intensity distribution. It has been previously shown that the propagation of such beams can be predicted using the FGBHM model [1] in which a standard FGB model as described by (1) is superposed with an *inverted* FGB model (the so-called constructed FGB) to create central shadow [1].

In the near field, when $z = 0$, the *inverted* FGB is written as

$$\psi_B(r,0) = A\sum_{n=0}^{B} C_n^B L_n\left(\frac{2Br^2}{v_0^2}\right)\exp\left[\frac{-Br^2}{v_0^2}\right]$$
$$= A\sum_{n=0}^{B}\exp\left(-\frac{Br^2}{w_0^2}\right)\frac{\left(Br^2/w_0^2\right)^n}{n!}, \quad B = 1, 2, 3, \ldots \tag{2}$$

where

$$C_n^B = (-1)^n\sum_{m=n}^{N}\binom{m}{n}\frac{1}{2^m} \tag{3}$$

The spot size v_0 of this beam is related to the spot size of FGB through a variant factor ε since $v_0 = \varepsilon w_0$. B is the beam order of the *inverted* FGB, which controls the steepness of the shoulders of the hole. The propagation of the *inverted* FGB is similar to the standard FGB model, considering the near-field beam diameter of the Laguerre–Gaussian function, $v_B(0)$, which is related to the width of the standard FGB through (see ref. 2)

$$v_B(0) = \frac{v_0}{\sqrt{B}} \tag{4}$$

The superposition of the two FGBs is thus,

$$\psi_{ur}(r,z) = \psi_N(r,z) + \eta\psi_B(r,z) \tag{5}$$

where η is a variable constant that enables various spatial intensity distributions to be achieved [1].

3. Evolution of copper laser beam quality

A common type of laser used for micromachining that employs URs is the copper vapour laser (CVL). CVLs with URs are described as multipass amplifiers of an initial burst of seed radiation, rather than being true laser oscillators with optical modes dependent on a set of boundary conditions [2]. Indeed, the short gain duration (20–80 ns) of CVLs generally restricts the propagation of laser radiation to a total of 2 to 5 round-trips within the resonator. The relatively small number of round-trips is insufficient to generate high beam quality output from a CVL employing a plane–plane resonator (high beam quality is defined as laser light exhibiting high transverse coherence and low divergence, typically less than 1 mrad). It has been shown that the beam quality of CVL output can be significantly improved by employing high-magnification URs [12] (the magnification, M, is defined as the ratio of the radius of curvature of the high reflector R to the radius of curvature of the spot reflector r ($M = R/r$) in the oscillator, as shown in Fig. 1).

CVL beam quality has been shown to evolve in a stepwise fashion [2]. Therefore, the beam quality is dependent on the number of round-trips that the radiation undergoes as it passes through the gas medium. The pulse laser shown in Fig. 2 exhibits characteristic intensity modulations corresponding to radiation that has undergone successive round-trips through the UR.

The initial output shown in Fig. 2, designated as *low beam quality* output, includes the highly divergent amplified spontaneous emission (ASE) originating from the output that has undergone less than one round-trip through the resonator. Subsequent output is loosely termed *high beam quality* output and includes radiation that has undergone two or more round-trips through the resonator. In this discussion, the *high beam quality* component is further divided into two subcategories, namely, *low divergent* output and *near-diffraction limited* output (within 2× of the diffraction limit).

Fig. 1. (*a*) Oscillator in an unstable resonator. (*b*) An on-axis unstable, confocal resonator.

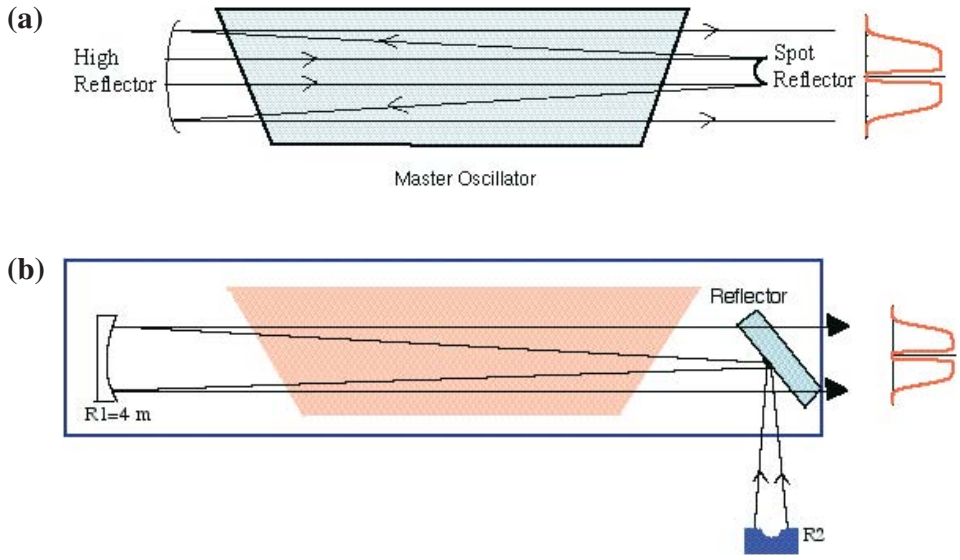

Fig. 2. Characteristic intensity modulations corresponding to round-trip time in the resonator of a copper vapour laser.

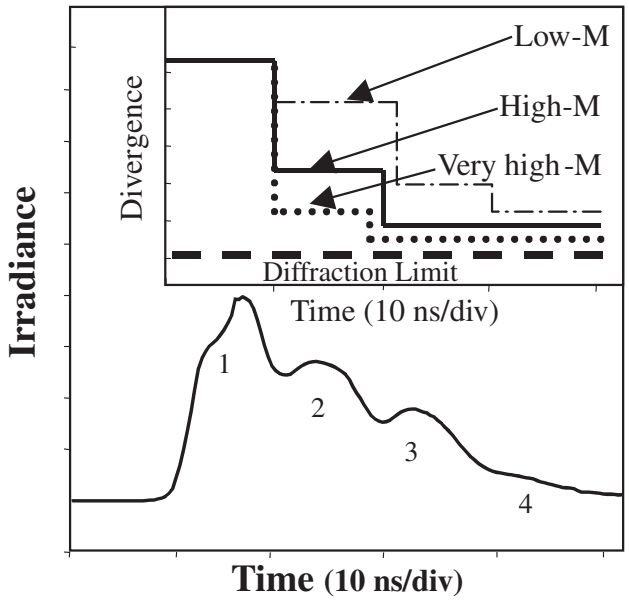

The magnification of the resonator influences the rate at which the divergence of each round trip approaches the diffraction limit. Low-magnification cavities ($M \ll 100$) can take four and more round-trips to produce near-diffraction limited output. In this case, the output consists of many different divergence components. By comparison, high-magnification cavities ($M = 100$) have been shown to produce near-diffraction limited output after three round-trips through the resonator, when used with a 25 mm diameter CVL [12].

In this case, the *high beam quality* output can be clearly divided into *low divergence* (radiation having undergone two round-trips) and *near-diffraction limited* components (three or more round-trips). Very high-magnification cavities ($M \gg 100$) can produce *near-diffraction limited* output after just two round-trips, however, and this results in decreased cavity feedback that ultimately reduces laser output power (and increases sensitivity to perturbation by spurious reflections from external optical elements). In this case the *high beam quality* component consists of only *near-diffraction limited* output.

The FGBHM model uses a combination of a paraxial approximation theory term and a geometric correction term derived by using simple ray-tracing to simulate beam characteristics. In this paper, the FGMHM model is used for both the simple case of very high magnification ($M = 400$), where the high beam quality component of laser output consists entirely of near-diffraction limited output, and more complex cases of lower magnifications ($M = 200$, and 80), where additional low divergent components are present. *Note that although highly divergent ASE is also present, it is lost rapidly in any practical situation and is consequently ignored in the model.*

4. Defining the total angle of divergence using the beam propagation factor

Although the material of this section is explained in detail in ref. 1, for the sake of the other sections, we give a summary. Using the IMF method, the theoretical values of the beam propagation factor M^2_{theor} can be derived for different beam orders. For convenience, *we shall consider only rectangular symmetry but the results can be readily transposed to the cylindrical case*. If the complex field amplitude at the waist of a symmetrical beam in rectangular coordinates is written as M^2_{theor}, the beam width after normalizing in the near field can be defined using the IMF method as,

$$w^2_{\text{near field}} = \frac{\int_{-\infty}^{\infty} |\psi(x,0)|^2 x^2 \, \mathrm{d}x}{\int_{-\infty}^{\infty} |\psi(x,0)|^2 \, \mathrm{d}x} \tag{6}$$

where $|\psi(x,0)|^2$ is the intensity profile in the near field and a similar equation holds for the far-field distribution

$$w^2_{\text{far field}} \hat{=} \frac{\int_{-\infty}^{\infty} |\tilde{\psi}(\rho)|^2 \rho^2 \, \mathrm{d}\rho}{\int_{-\infty}^{\infty} |\tilde{\psi}(\rho)|^2 \, \mathrm{d}\rho} \tag{7}$$

where $|\tilde{\psi}(\rho)|^2$ is the intensity profile in the far field.

Considering the Fourier optics,

$$\int_{-\infty}^{\infty} |\psi(x)|^2 \, \mathrm{d}x = \int_{-\infty}^{\infty} |\tilde{\psi}(\rho)|^2 \, \mathrm{d}\rho \tag{8}$$

and

$$\int_{-\infty}^{\infty} |\tilde{\psi}(\rho)|^2 \rho^2 \, \mathrm{d}\rho = \int_{-\infty}^{\infty} \left| \frac{\mathrm{d}\psi(x)}{\mathrm{d}x} \right|^2 \mathrm{d}x \tag{9}$$

Fig. 3. The extension of the beam divergence angle for $M = 80$, 200, and 400.

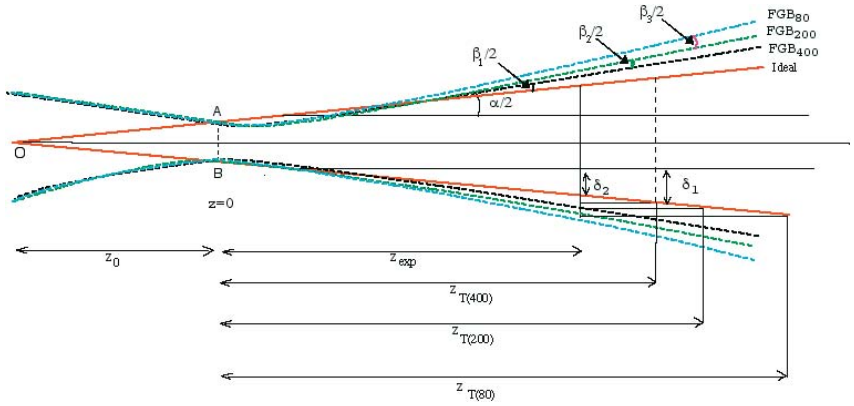

the beam propagation factor, using the far- or near-field distributions, can be defined by (see refs. 3 to 7)

$$M_x^2 = \frac{\sqrt{\left(\int_0^\infty |\psi(x,0)|^2 x^2\,\mathrm{d}x\right)\left(\int_0^\infty \left|\frac{\mathrm{d}\psi(x,0)}{\mathrm{d}x}\right|^2 \mathrm{d}x\right)}}{\int_0^\infty |\psi(x,0)|^2\,\mathrm{d}x} \tag{10}$$

For the sake of simplicity, we just consider the x coordinate $\left(M_x^2 = M^2 = M_{\text{theor}}^2\right)$. However, for systems that use a lens of focal length f to image the far field, a useful well-known equation used to derive the beam propagation factor experimentally is (see ref. 5)

$$M_{\text{expt}}^2 = \frac{\pi d_0 D_0}{4\lambda f} \tag{11}$$

where d_0 and D_0 are the beam diameters of the beam in near and far fields. The angle of divergence θ in the paraxial regime is given by

$$\theta = \frac{4\lambda M^2}{\pi d_0} \tag{12}$$

where M^2 is the beam propagation factor. Substituting M_{theor}^2 or M_{expt}^2 for M^2 allows the full angle of divergence to be calculated for the theoretical and experimental cases. Ideally, $M_{\text{theor}}^2 = M_{\text{expt}}^2$, however, discrepancies arise because the real laser beam consists of different output components having undergone two or three round-trips with angles of divergence larger than the diffraction limit as defined by (8). Practically, the beam divergence angle is described by the sum of the angle of divergence in the diffraction limit regime $\alpha = \left(4\lambda M_{\text{theor}}^2\right) / (\pi d_0)$ and an additional angle β, representing the angle of divergence above the diffraction limit, which is used for the more divergent components in the real laser beam (see Fig. 3). This is dealt with in the model by using an effective propagation distance z_{theor} in place of the real propagation distance z_{expt}. The full-aperture diffraction limited beam would evolve the same beam diameter in distance z_{theor} as does the real laser beam in distance z_{expt}. However, a tool that enables us to estimate the beam intensity distribution at any arbitrary plane is obtained using a constructed z instead of real z (due to the higher angle of divergence in the experiment, the beam spot diameter at any arbitrary plane of measurement is bigger than the one predicted by theory (see Fig. 3)).

Geometrical optics enables us to find the relation between z_{expt} and z_{theor}

$$\tan\left(\frac{\alpha}{2}\right) = \frac{\delta_2}{z_{\text{expt}}} = \frac{\delta_1}{z_{\text{theor}}} \tag{13}$$

where $\alpha/2$ is the angle of divergence in the paraxial regime and AB is the diameter of the aperture. The beam diameter at z_{expt} (in the experimental case) is given by

$$w_{\text{expt}} = \text{AB} + 2z_{\text{expt}} \tan\left(\frac{\alpha+\beta}{2}\right) \tag{14}$$

An identical beam diameter to the one described by (13) can be achieved in the paraxial approximation regime at z_{theor} by

$$w_{\text{expt}} = \text{AB} + 2z_{\text{theor}} \tan\left(\frac{\alpha}{2}\right) \tag{15}$$

It follows that

$$\begin{aligned} z_{\text{theor}} =& \frac{\text{AB}}{2\tan(\alpha/2)} \left\{ \frac{\text{AB} + 2z_{\text{expt}} \left[\frac{\tan(\alpha/2)+\tan(\beta/2)}{1-\tan(\alpha/2)\tan(\beta/2)}\right]}{\text{AB} + 2z_{\text{expt}} \tan(\alpha/2)} - 1 \right\} \\ &+ \frac{\text{AB} + 2z_{\text{expt}} \left[\frac{\tan(\alpha/2)+\tan(\beta/2)}{1-\tan(\alpha/2)\tan(\beta/2)}\right]}{\text{AB} + 2z_{\text{expt}} \tan(\alpha/2)} z_{\text{expt}} \end{aligned} \tag{16}$$

or

$$z_{\text{theor}} = \frac{z_{\text{expt}} \left[\tan(\beta/2) + \tan(\alpha/2)\right] + \frac{2}{\text{AB}} z_{\text{expt}}^2 \tan(\alpha/2) \left[\tan(\alpha/2) + \tan(\beta/2)\right]}{\tan(\alpha/2) \left[1 - \tan(\alpha/2)\tan(\beta/2)\right] \left[1 + \frac{2}{\text{AB}} z_{\text{expt}} \tan(\alpha/2)\right]} \tag{17}$$

where α and β are considered to be small, $\tan(\alpha/2) = \alpha/2$, and $\tan(\beta/2) = \beta/2$.

When $(\alpha/\text{AB}) z_{\text{expt}} \ll 1$ and $\frac{1}{(1+(\alpha/\text{AB}) z_{\text{expt}})} \approx \left(1 - (\alpha/\text{AB})\, z_{\text{expt}}\right)$ then (17) becomes

$$z_{\text{theor}} \cong \frac{3}{\alpha\left(1 - \alpha\beta/4\right)} \left[z_{\text{expt}} (\alpha+\beta) - \frac{\alpha}{\text{AB}} z_{\text{expt}}^2 (\alpha+\beta) \right] \tag{18}$$

In the limit of z_{expt}, the scaling formula collapses to a more simplified format

$$z_{\text{theor}} = \frac{3(\alpha+\beta) z_{\text{expt}}}{\alpha\left(1 - \alpha\beta/4\right)} \tag{19}$$

5. Kurtosis factor

The kurtosis factor k (also called the shape parameter) describes the flatness (or sharpness) of the irradiance distribution compared to normal Gaussian beams and is independent of the beam radius and divergence. It can be expressed in terms of the second and fourth moments of the normalized field (see refs. 8 and 9)

$$k = \frac{\left(\int_0^\infty |\psi(x,z)|^2 x^4 \, \mathrm{d}x\right) \left(\int_0^\infty |\psi(x,z)|^2 \, \mathrm{d}x\right)}{\left(\int_0^\infty |\psi(x,z)|^2 x^2 \, \mathrm{d}x\right)^2} \tag{20}$$

It has been demonstrated that the kurtosis is related to the beam order in the standard FGB model through (see ref. 1)

$$N = \sqrt{\frac{\frac{3}{2}}{\left(k_{\mathrm{FGB}} - \frac{9}{5}\right)^2} - \frac{3}{2}\sqrt{k_{\mathrm{FGB}} - \frac{9}{5}} + \left(k_{\mathrm{FGB}} - \frac{9}{5}\right)} \tag{21}$$

with $\Delta N = \pm 1$.

Furthermore, it was shown that at $z = 0$, the kurtosis of the FGB model is related to the FGBHM model through (see refs. 1 and 2)

$$k_{\mathrm{FGB}} = k_{\mathrm{FGBHM}} + 2\varepsilon \tag{22}$$

where ε is a variant-constant parameter that is obtained using the unitless numerical value of the hole diameter [1]. Thus, by measuring the k_{FGBHM} and knowing ε, we are able to obtain k_{FGB} and consequently N using (22).

6. Experimental set-up

The laser used in this study was a conventional 15 W CVL (active volume of 25 mm diameter by 1 m long) with a thyratron switched excitation circuit consisting of two stages of pulse compression. The laser was operated with a 2% H_2–Ne buffer gas (buffer gas pressure of 40 Torr (1 Torr = 133.3224 Pa)) at a pulse repetition frequency of 10 kHz.

The optical resonator for the present experiment was an on-axis, positive-branch, unstable, confocal resonator formed by a $R_1 = 4$ m high reflector (50 mm diameter) at one end, with a 1 mm diameter scraper mirror directing the centre of the beam onto an auxiliary reflector at the other end. The auxiliary reflectors investigated had radius of curvatures R_2, of 1, 2, and 5 cm, corresponding to resonator magnifications (R_1/R_2) of $M = 400$, 200, 80, respectively (see Fig. 1). In each case, the beam was collimated using a collimator tester by adjusting the distance between R_2 and the scraper mirror.

6.1. Near field

Pulse-averaged near-field irradiance profiles of the green component of laser output were recorded by using a dichroic filter to reject the yellow component and the imaging was done using a $f = 160$ mm achromatic lens onto the CCD camera (TM 745) of a laser beam analyser (Spiricon LBA-PC). Once optimized using the knife edge method, this imaging configuration was fixed to an optical rail to ensure self-consistency in measuring beam profiles. Near-field intensity profiles were recorded at different positions along the propagation axis, namely, $z = 0$ (corresponding to the plane immediately behind the output coupler), 1, 2, 5, and 15 m.

6.2. Far field

Pulse-averaged far-field intensity profiles of the green laser output were examined by taking a low-power sample of the output (via reflections from several wedges), and then bringing this sample to focus using a $f = 750$ mm achromatic doublet. A magnified image of this focal spot was produced on the CCD camera of the laser beam analyser using a $f = 75$ mm singlet lens. Note, for most applications the ASE would be removed from the beam by spatial filtering, however, to avoid introducing additional aberrations, the beam was not spatially filtered in these experiments. Nevertheless, as previously stated, ASE is lost rapidly and is not discernible in the far-field intensity profiles.

Fig. 4. The intensity profiles for $M = 80$, 200, and 400 (near field).

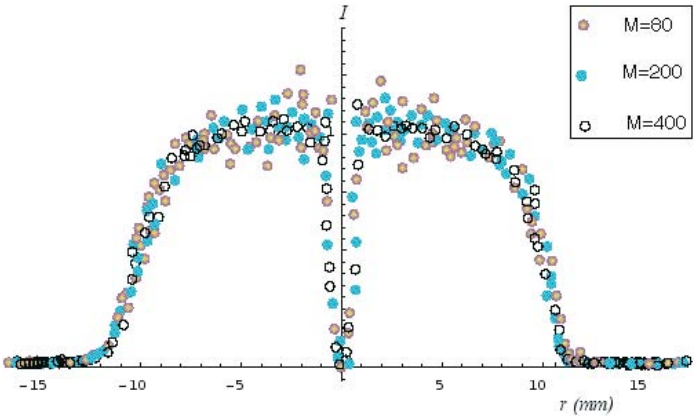

Fig. 5. The intensity profiles for $M = 80$, 200, and 400 (far field).

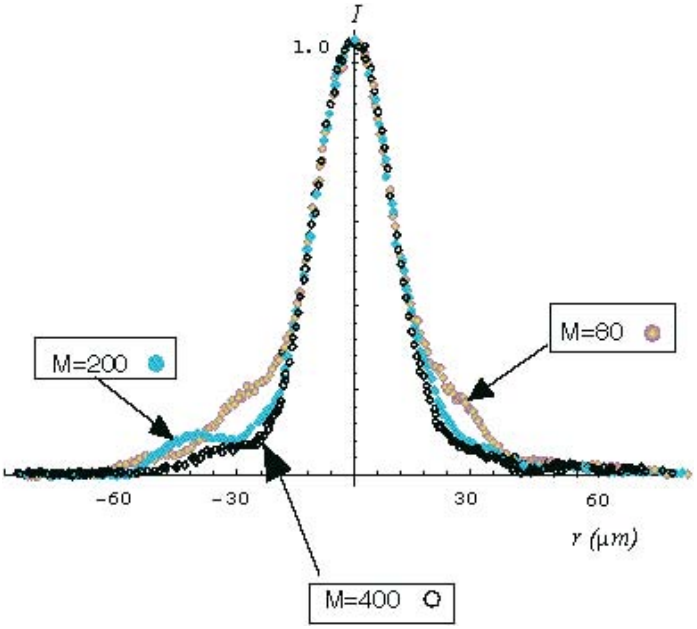

7. Results and discussion

As discussed above, the output beam of the CVL using an UR with $M = 400$ (very high magnification) consists predominantly of just two components, ASE and near-diffraction limited output (high beam quality or low divergence). For $M = 400$, the far field consists almost entirely of near-diffraction limited output and presents a simple case for testing the model. As M decreases, additional high-divergence components appear in the output beam and provide a useful test for the model over a range of conditions ($M = 200$ and 80).

It must be noted that, at $z = 0$ (the first plane of measurement), the differences between the output intensity profiles for the three magnifications are negligible (see Fig. 4). However, their differences are quite pronounced in the far field (see Fig. 5). The far-field distributions in these three cases all share a dominant central peak. For $M = 400$, the wings approximate an Airy disk distribution. However, for the $M = 200$ resonator, the wings on either side become larger, indicating larger contributions from the

Table 1. Theoretically evaluated beam quality parameters.

	Units	$M = 400$	$M = 200$	$M = 80$
$\alpha = 4\lambda M^2_{\text{theor}}/\pi d_0$	μrad	264	264	264
w_0	mm	26	26	26
$W_{\text{far field}}$	μm	105	120	140
$M^2_{\text{expt}} = 4\pi d_0 D_0/\lambda f$	—	5.61	6.41	7.47
$\theta = \alpha + \beta$	μrad	280	320	373
β	μrad	16	56	109

more divergent components. This effect is more pronounced for the $M = 80$ case, where these wings are washed out, giving the impression of a larger beam diameter. Using our measurements in the near and far fields, M^2 and thus, the angle of divergence, can be calculated. As mentioned above, at $z = 0$ there is no significant difference between the intensity profiles for the three different magnifications, so the kurtosis factor is almost identical for the three cases and from the measured data k is determined to be 1.83. The radius of the central shadow is measured to be ~0.5 mm (at $z = 0$), ε has the value of 0.05 ($\varepsilon = N[d]/10$), where $N[d]$ is the numerical unitless value of the radius of the central shadow. The kurtosis value in the near field for the standard FGB with the same beam order can be defined using (22) as 1.84 and from (21) $N = 30 \pm 1$.

The beam parameters $N = 30$, $B = 3$, $\eta = -1$, and $\varepsilon = 0.05$ give a theoretical value for the beam propagation factor M^2 of 5.28. To evaluate the FGBHM model, we need to first measure the beam width in two planes along the z-axis (typically at the near and far fields). Following the same method as described in ref. 2, the angle of divergence in the theoretical and experimental regimes can be determined. This information is tabulated in Table 1. For the $M = 400$ case, the small value of β indicates that the deviation from an ideal beam in the paraxial approximation regime is minimal and that the output beam is almost (but not entirely) near-diffraction limit radiation.

The scaling equations and the constructed z for every plane of measurements (at z_{expt}) can be readily obtained. Comparisons between the beam intensity profiles in the near fields, with the theoretical intensity distribution at $z = 0$, 1, 2, 5, 15 m, are illustrated in Fig. 6 for magnifications of 400, 100, and 80. The differences between the output intensity profiles at $z = 0$ (see Fig. 5) and $z = 1$ m (see Fig. 7) for this range of magnifications is insignificant. However, at $z = 2$ m, the differences between the beam intensity profiles produced by URs having different magnifications are clearly apparent. For the $M = 400$ case, at $z = 2$ m, a central peak has appeared. In contrast, for both the $M = 200$ and 80 cases, a central trough is observed at $z = 2$ m. The FGBHM model also predicts that for $M = 200$ the depth of the central trough is less than in the $M = 80$ case, as is clearly observed. At $z = 5$ m, the intensity profiles of the three conditions have similar distributions (a central trough and two peaks), however, for $M = 400$ the two peaks are flatter than the other cases and the degree of flatness decreases from $M = 200$ to 80. Similarly, at $z = 15$ m, the shoulders of the intensity distributions for these URs lose their flatness entirely and become sharp. The central trough indicated at $z = 5$ m is replaced by a small peak.

The model shows excellent agreement with the simple case where the output pulse largely consists of one near-diffraction limited component at a resonator magnification of $M = 400$. However, the model also predicts, to a high degree of accuracy, laser beam evolution when the output pulse consists of a number of components that diverge at different rates as the beam propagates through space. This result has important implications for modelling beam evolution for a wide range of laser types.

Fig. 6. A comparison between the beam intensity profiles in the near field, with the modelled intensity distribution at $z = 0$, 1, 2, 5, 15 m.

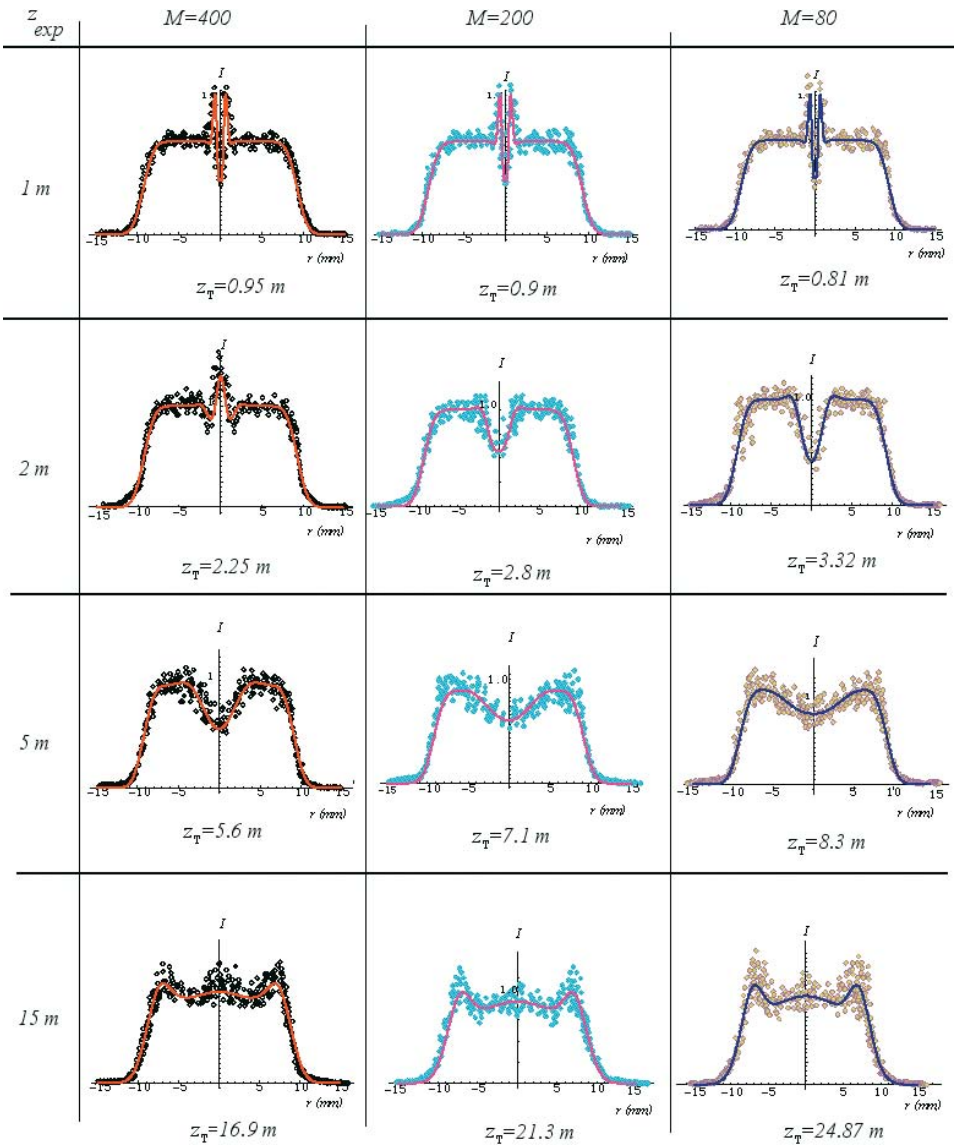

8. Summary

The FGBHM model with constructed z enables us to predict the intensity profiles at any plane along the z-axis. It was demonstrated that the beam parameters can be defined by measuring the intensity profile *in just two planes along the propagation axis (near field, $z = 0$, and far field)* and that the comparison between the theoretical predictions (the continuous line) and the measured data (dots) indicates excellent agreement between theory and experiment. It was demonstrated that even for lasers employing unstable resonators with low to medium magnification, this model is capable of predicting useful information about the beam shape, angle of divergence, and the beam diameters at any point along the z-axis that would be used by laser physicists, industrial workers, or medical doctors. We used

Fig. 7. (*a*) Patient with a port wine stain before treatments. (*b*) After treatments of the patient with reconstructed semi-flat-top beam (after 7 m propagation).

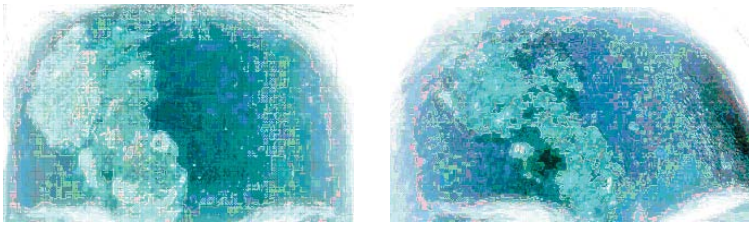

(a) Before treatments (b) After treatments with flat-top beam

our results in medical research for removing port wine stains (PWSs) of different sizes, employing our CVL (green as well as yellow), and it can be seen from Fig. 6 that our flat-top beams having a hole in the middle, after propagating a few metres, start to lose that hole and become semi-flat (in all three cases). Using optical instruments, we have been able to produce semi-flat-top beams and have used them for medical purposes, such as removing PWSs of various sizes, and great results have been achieved, as shown in Fig. 7. Figure 7*a* demonstrates a patient with a large PWS (lighter color shows deeper PWS) after five treatments with semi-flat-top beam using copper vapor laser (578 nm, 6 W, 4 mm spot-size). A great improvement have been achieved and the area of lighter color area has been decreased significantly.

Acknowledgment

The authors thank Islamic-Azad University, Iran Research and Science Foundation and Macquarie University for the support given to this work.

References

1. S. Saghafi, M.J. Withford, and J.A. Piper. J. Opt. Soc. Am. A, **18**, 7, 1634 (2001).
2. D.J.W Brown and J.A. Piper. Appl. Opt. **32**, 2058 (1993).
3. D.R. Hall and P.E. Jackson. The physics and technology of laser resonators. Adam Hilger, Bristol, New York. 1989. pp. 132–142.
4. A.E. Siegman. Proc. SPIE. **1224**, 2 (1990).
5. T.F. Johnston. Laser Focus World, **26**, 173 (1990).
6. ISO/TC 172/SC9/WG1/N56. Optics and optical instruments: test methods for laser beam parameters. 1996.
7. A.E. Siegman. Trends Opt. Photonics, 123 (1998).
8. R. Martinez-Herrero, G. Piquero, and P.M. Mejias. J. Opt. Commun. **115**, 225 (1995).
9. R. Martinez-Herrero, P.M. Mejias, M. Sanchez, and J.L.H. Neira. IEEE J. Opt. Quantum Electron. **24**, 1021 (1992).
10. M. Scholl and G. Herizger. Proc. SPIE. **2375**, 130 (1995).
11. F. Gori. J. Opt. Commun. **107**, 335 (1994).
12. K.I. Zemskov, A.A. Isaev, M.A. Kazaryan, G.G. Petrash, and S.G. Rautian. J. Elek. **11**, 863 (1974).